

Research paper

3D printed CoCrMo personalised load-bearing meta-scaffold for critical size tibial reconstruction

Chameekara T. Wanniarachchi^{a,b}, Arun Arjunan^{a,c,*}, Ahmad Baroutaji^d, Manpreet Singh^{a,e}, John Robinson^{a,f}, Aaron Vance^{a,c}, Martin Appiah^a, Abul Arafat^a

^a Additive Manufacturing of Functional Materials Research Group, University of Wolverhampton, Telford, TF2 9NT, UK

^b Aceon Group Ltd., Stafford Park 12, Telford, TF3 3BJ, UK

^c University hospitals of Derby and Burton NHS foundation trust, Derby, DE22 3NE, UK

^d School of Engineering and Technology, College of Engineering and Physical Sciences, Aston University, Birmingham, B4 7ET, UK

^e Elite Centre for Manufacturing Skills (ECMS), University of Wolverhampton, Springfield Campus, WV10 0JP, UK

^f Additive Analytics Ltd., Stirchley Road, Telford, TF3 1EB, UK

ARTICLE INFO

Keywords:

Additive manufacturing
Laser-powder bed fusion
Metamaterials
Meta-biomaterials
Negative Poisson's ratio
Auxetic
Bone scaffold

ABSTRACT

Porous scaffolds have evolved, allowing personalised 3D-printed structures that can improve tissue reconstruction. By using scaffolds with specific porosity, Poisson's ratio and stiffness, load-bearing tissues such as tibial reconstruction can be improved. Recent studies suggest the potential for negative Poisson's ratio ($-v$) meta-scaffolds in mimicking the behaviour of natural tissue, leading to improved healing and tissue reintegration. This study reveals a porous meta-scaffold that offers high $-v$ and can be personalised to match desired stiffness. By using laser powder bed fusion (L-PBF) of CoCrMo, a porous structure was created, characterised by its ability to achieve heightened $-v$. Prototype testing and numerical modelling unveiled a proxy-model capable of predicting and personalising the porosity, yield strength, elastic modulus, and $-v$ of the tibial meta-scaffold representing a novel contribution to the field. The surrogate model also aids characterising the impact of design variables such as of the scaffold on the key performance requirements of the tibial scaffold. This approach enables the fabrication of porous biomaterials with personalised properties, specifically suited for load-bearing tibial reconstruction. The resulting meta-scaffold offers $-v$ ranging from -0.16 to -0.38, porosity between 73.46% and 85.36%, yield strength of 30–80 MPa, and elastic modulus ranging from 8.6 to 22.6 GPa. The optimised architecture feature $-v$ of 0.223 and a targeted elastic modulus of 17.53 GPa, while also showcasing yield strength and porosity of 57.2 MPa and 76.35%, respectively. By combining 3D printing with tailored scaffolds, this study opens doors to mass customisation of improved load-bearing porous biomaterials that of negative Poisson's ratio and stiffness matching.

1. Introduction

Tissue reconstruction has witnessed significant advancements with the incorporation of biomaterials, providing a scaffold for cell growth and tissue development [1–3]. These biomaterials can be tailored to meet specific requirements, such as mechanical strength, biodegradability, and biocompatibility. amongst the diverse biomaterials, porous biomaterials engineered at the nanoscale have gained prominence due to their unique properties and tunability for various biomedical applications [4,5].

Subsequently, these rationally designed meta-biomaterial architec-

tures hold significant promise in load-bearing tissue engineering due to their ability to mimic the hierarchical structure and mechanical properties of native tissues, thus enhancing tissue regeneration and integration [6]. These architectures encompass a variety of advanced fabrication techniques and materials, enabling precise control over structural design and mechanical properties to match those of the target tissue. By integrating multiple materials at different length scales, such as nanofibers, microspheres, and macroscale scaffolds, meta-biomaterials can achieve tailored mechanical properties, porosity, and degradation rates [7]. This versatility allows for the creation of scaffolds that closely mimic the complex architecture of load-bearing

* Corresponding author.

E-mail address: a.arjunan@wlv.ac.uk (A. Arjunan).

<https://doi.org/10.1016/j.stlm.2024.100163>

Received 12 February 2024; Received in revised form 6 May 2024; Accepted 15 May 2024

Available online 22 June 2024

2666-9641/© 2024 The Authors. Published by Elsevier Masson SAS. This is an open access article under the CC BY license (<http://creativecommons.org/licenses/by/4.0/>).

tissues like bone, cartilage, and tendon, promoting cell attachment, proliferation, and differentiation [8,9]. Notably, $-v$ porous biomaterials offer intriguing potential for tissue regeneration [10,11]. Their ability to become thicker in the transverse direction during stretching makes them suitable for creating implants that better conform to surrounding tissues [12,13].

Research on the fabrication and application of $-v$ biomaterials have been extensively explored in the field of tissue reconstruction. Examples include the development of functionally graded $-v$ polymer structures for femoral hip replacement [9]. By achieving a mechanical similarity to the host bone, stress mismatch and implant loosening were mitigated, indicating the potential of $-v$ biomaterials in hip replacement. Stress shielding and maladapted stress concentration have been identified as significant issues in bone tissue engineering [10–12,14–16]. Studies have confirmed that a large mismatch in stiffness between the host bone and the load-bearing implant leads to these complications [17,18]. To address this, researchers have focused on $-v$ biomaterials with high proliferation and tissue reintegration capabilities [7,19]. By controlling v in porous materials, the strain stimulus during bone regeneration can be manipulated [20,21], influencing the overall tissue reconstruction process [22].

Mechanical stimulation has been recognised as a key regulator of bone regeneration and healing [23,24]. The ability of $-v$ materials to offer mechanical properties tailored to natural tissue has shown promise in improving tissue reconstruction [25]. Moreover, high strains have been found to promote faster regeneration in fibrous tissues [26]. Thus, $-v$ biomaterials with high $-v$ may offer extended mechanical stimulus, potentially enhancing tissue reintegration [27,28].

The role of porosity in bone scaffolds cannot be underestimated, as it influences cell distribution and nutrient supply to grafted and replenished cells [29,30]. Additive manufacturing (3D printing) technologies have enabled the fabrication of personalised porous scaffold biomaterials, offering a suitable approach for patient-specific implants and bone scaffolds [31–37]. The integration of additive manufacturing in this context has the potential for mass personalisation, revolutionising the field [38,39]. Considering the challenges associated with stress-shielding and maladapted stress concentration, the question arises: What properties should be targeted to achieve a higher $-v$ in porous biomaterials? The stiffness (elastic modulus) matching between implants and host bone is crucial [40–43]. This research proposes the conception of a high $-v$ porous biomaterial optimised to attain a targeted stiffness of approximately 18 GPa mimicking an adult tibial critical size section while preserving other essential parameters for bone scaffolds [44–46].

For load-bearing implants such as complete joint prostheses (artificial joints) for elbows, shoulders, knees and ankles, metals and alloys have been commonly used, as well as for prosthetic devices, such as frames, pins, and screws [17]. Metals have tight inter-atomic bonds that, in response to standard compressive strength, offer heightened mechanical properties and impact resistance, so generally they bend without cracking under high loads. However, under the complex physiological and metabolic characteristics of biological cells, they have poor resistance to corrosion [18]. With the exception of commonly used pure titanium, owing to its superior mechanical properties, such as hardness and corrosion tolerance, alloys are more widely used than metallic materials. Common biomaterials used for metallic orthopaedic implants are alloys of titanium, cobalt-chromium and stainless steels 316 and 316 L [19], with the mechanical properties as summarised in Table 1.

Titanium alloys are frequently employed in the development of porous bone scaffolds; however, Cobalt-chromium-molybdenum (CoCrMo) superalloy has been chosen as the biomaterial of choice in this study because of its high Young's modulus and density, leading to superior stiffness performance. This, in turn, allows for a significant opportunity to develop highly porous structures that can reduce stress-shielding effects associated with highly stiff implants.

The use of CoCrMo as the bulk material ensures high porosity while

Table 1

Mechanical properties of metallic biomaterials used for load-bearing implants [14].

Material	Elastic modulus (GPa)	Yield strength (MPa)	Tensile strength (MPa)
Cortical bone	15–30	30–70	70–150
Stainless steel	190	221–1213	586–1351
Co-Cr alloy	210–253	448–1606	655–1896
Titanium (Ti)	110	485	760
Ti alloy	116	896–1034	965–1103

maintaining load-bearing ability, critical for functional bone scaffolds. The meta-scaffold design parameters are algorithmically modified to achieve specific $-v$, stiffness, strength, and relative density using a validated surrogate model. The resulting meta-scaffolds offers high $-v$ while providing stiffness matching for patient-specific scenario, presenting a promising avenue for tissue reconstruction. Despite the rise of designer biomaterials, there is still a lack of porous biomaterial architectures that offer the high $-v$ while providing targeted stiffness matching [47–51]. To address this gap, this paper presents an open framework for the L-PBF of high $-v$ porous biomaterial meta-scaffolds for tibial reconstruction.

2. Material and methods

2.1. CoCrMo

The CoCrMo feedstock used for the laser powder bed fusion (L-PBF) process had a composition consisting of Co, Cr, Mo, and trace amounts of Si, Mn, Fe, C, and Ni, as indicated in Table 2. With a density of 8300 kg/m³, the feedstock largely features spherical morphology for LPBF as shown in Fig. 1a and 1b. Occasional presence of elongated particles were also found with attached satellite particles as shown in Fig. 1a. However, they were typical of CoCrMo L-PBF feedstock used for dense fabrication and does not signify the overall quality of the feedstock. The feedstock generally exhibited a spherical shape, with particle sizes ranging from 7.33 to 47.66 μm as summarised in Fig. 1b, with majority of the particle sizes falling below 22 μm .

2.2. Meta-scaffold design and fabrication

Efforts to develop materials with $-v$ have driven the exploration of re-entrant architectures, offering an efficient path to achieve the desired behaviour. Amongst these architectures, the chevron or bowtie design has gained recognition for its high $-v$ properties [52–54]. This work builds on previous research [55] that highlighted the advantages of the current re-entrant meta-scaffold in contrast to other auxetic patterns. In the field of tissue engineering, particularly in the context of bone scaffolds, the selection of an appropriate architectural design is pivotal for achieving optimal mechanical properties and cellular responses conducive to tissue regeneration. Amongst various auxetic architectures, re-entrant structures have emerged as a promising candidate due to their unique geometric features, which offer distinct advantages over traditional designs.

Firstly, re-entrant structures exhibit superior mechanical properties compared to other auxetic architectures. This assertion finds support in studies by Gibson and Ashby [56], who investigated the mechanical behaviour of cellular solids and highlighted the significance of geometry in determining material properties. The inward bending nature of the re-entrant architecture enables the distribution of mechanical loads more effectively, thereby mitigating stress concentrations and enhancing overall toughness and resilience. This mechanical robustness is crucial for bone scaffolds, where the material must withstand

Table 2
Chemical composition of the CoCrMo alloy used for l-PBF.

Elements	Co	Cr	Mo	Si	Mn	Fe	C	Ni
Comp. (wt.%)	60–65	26–30	5–7	≤1.0	≤1.0	≤0.75	≤0.16	≤0.1

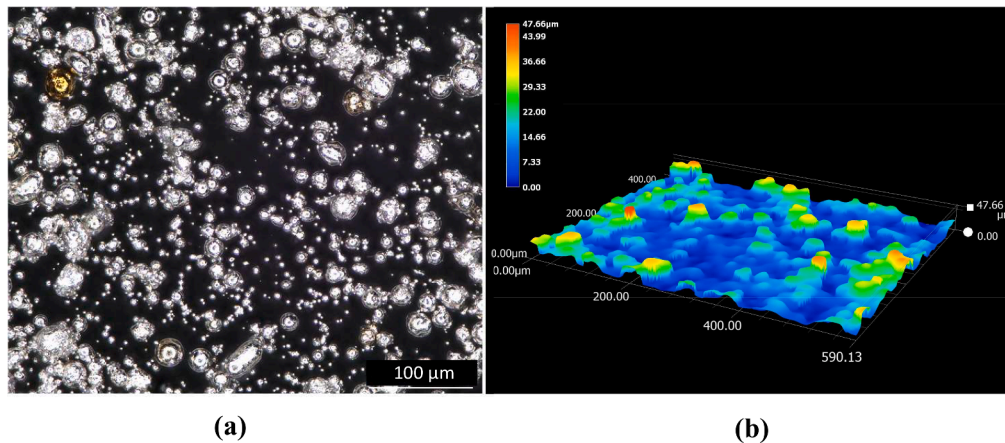


Fig. 1. Microscopic analysis of CoCrMo used for l-PBF showing (a) particle shape and (b) particle size.

physiological forces while providing a supportive environment for tissue ingrowth.

The re-entrant architecture also offers enhanced porosity control and interconnectivity, which are essential for facilitating cell infiltration, nutrient diffusion, and tissue regeneration within the scaffold. Studies by Kim et al. [25], who demonstrated that the intricate geometry of re-entrant structures enables precise tuning of pore size, shape, and distribution, thereby promoting optimal cellular responses. The ability to control porosity is particularly advantageous in bone tissue engineering, where proper vascularisation and nutrient supply are critical for successful tissue regeneration. According to Lee et al. [57], re-entrant architectures offer surface characteristics that promote cellular adhesion, proliferation, and differentiation. The curved surfaces and interconnected pores of re-entrant structures are suitable for cell attachment and interaction, thereby facilitating favourable cellular responses post-implantation.

Building upon existing research [55,58,59], this study adopts a re-entrant honeycomb structure to attain the desired $-v$ characteristics, as illustrated in Fig. 2a. The unit cells were assembled to establish interconnected porosity suitable for load-bearing tibial scaffolds, while minimising overhangs to facilitate laser powder bed fusion (L-PBF) without requiring additional support structures. Variable parameters for

strut thickness (t_s) and strut angle (θ_s) were employed, with values ranging from 0.25 to 0.35 mm and 65 to 75°, respectively. The meta-scaffold was then designed by arranging the unit cells in three dimensions to reconstruct an 18 mm adult tibial critical-size bone scaffold, as depicted in Fig. 2b. This dimension choice aligns with commonly encountered tibial critical-size bone defects [60–62].

The meta-biomaterial specimens underwent fabrication using the l-PBF method with an EOS M290 3D printer. The process parameters for building the meta-scaffolds were optimised, maintaining a laser power of 290 W, scan speed of 950 mm/s, and hatch distance of 0.11 mm, which remained constant throughout fabrication. A protective Argon atmosphere was employed in the print chamber during horizontal laser beam scanning to melt the CoCrMo particles. Following printing, all specimens underwent heat treatment at 1150 °C for six hours to ensure stress relief. The stress-relieved meta-scaffolds and tensile test samples were detached from the base plate using Wire Electrical Discharge Machining (EDM).

2.3. Numerical modelling

To examine the non-linear behaviour of $-v$ meta-scaffolds, a validated finite element (FE) model was utilised based on the surrogate

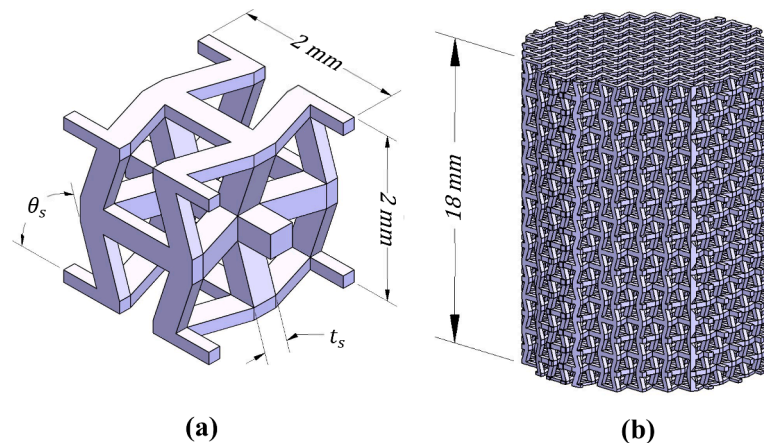


Fig. 2. Design evolution of the $-v$ porous biomaterial showing (a) the unit-cell shape and variable dimensions, (b) the resulting porous tibial meta-scaffold.

model. The most suitable material representation chosen for this study was the bilinear isotropic strain hardening (BISO) option. This representation assumes that the material has a linear region with a slope represented by the Young's modulus (E_{blk}) of the material, followed by a perfectly plastic post-linear region starting at bulk yield stress (σ_{blk}). All the numerical model's material parameters were experimentally derived from CoCrMo test specimens produced under the same conditions as the porous meta-scaffold. The analysis employed a 10-node higher-order tetrahedral element that offers quadratic displacement behaviour.

The BISO model is a constitutive material model used to describe the mechanical behaviour of materials subjected to deformation. It is commonly employed in finite element analysis (FEA) simulations to accurately predict the response of materials under various loading conditions. This model assumes that the material exhibits linear elastic behaviour up to a certain point, beyond which it undergoes strain hardening. In the initial stage of deformation, the material behaves elastically, obeying Hooke's law. This means that the stress is directly proportional to the strain, and the material will return to its original shape once the load is removed. The stiffness of the material in this region is characterised by E_{blk} , which represents the slope of the stress-strain curve. At a certain level of stress, known as the yield stress of the bulk material σ_{blk} , the material begins to undergo plastic deformation. For BISO, the yield point marks the transition from elastic to plastic behaviour beyond which the material experiences permanent deformation.

Post-yielding, the material undergoes strain hardening, where its resistance to further deformation increases with increasing strain. This phenomenon occurs due to microstructural changes within the material, such as dislocation movement and rearrangement. The BISO model assumes that the hardening behaviour can be represented by a linear increase in stress with respect to strain beyond the yield point. The stress-strain curve informing the BISO model feature two linear segments, the first one representing the elastic region followed by the strain hardening region. These two segments are connected at the yield point, forming a characteristic bilinear curve. The slope of the strain hardening segment represents the strain hardening modulus, which quantifies the rate at which the material becomes stronger with increasing plastic strain.

The model assumes that the material's mechanical properties are isotropic, meaning they are independent of the direction of loading. However, the 1-PBF process used to fabricate the meta-scaffold has the potential to introduce material anisotropy due to its layer-by-layer fabrication process. Several factors contribute to this anisotropy including microstructural variations, residual stresses, surface roughness. The use BISO model in the presence of material anisotropy is justified for current study due to the large amount of porosity featured in the architecture. Here the mechanical performance is largely driven the

porous micro-architecture reducing the influence of the relatively smaller material anisotropy that is featured in the bulk material.

During numerical modelling the first attempt is to selection the most simplistic material model and to evaluate its suitability during the validation cycle that in this case is informed by physical prototype testing. Table 6 informs that the numerical model convergence well within the experimental performance signified by a difference of 4.05% between the two methods. Therefore, using a BISO material model is considered appropriate as it offers simplicity in implementation and computational efficiency compared to more complex anisotropic models. Here, the directional dependence of the bulk material properties here can be deemed negligible and the BISO model provides a pragmatic compromise between accuracy and computational cost. Thus, while anisotropic models may provide greater fidelity to material behaviour, BISO model is suitable considering the validation accuracy and computational efficiency.

The crush plates were modelled as rigid bodies on the top and bottom surfaces of the meta-scaffold structure (Fig. 3a). The meta-scaffold was left unconstrained, free to rotate and deform in all directions. The loading process was conducted through 100 sub-steps to avoid spurious effects, and deformation was monitored at a high resolution. For the modelled end plates, the thickness was inconsequential as load transfer through them was not computed. The bottom plate was fixed in all directions, while the top plate was moved 10% of the meta-scaffold's height to simulate axial compression. The connection between the rigid bodies and the meta-scaffold was treated as frictional with a constant of 0.1 to simulate realistic behaviour. The accuracy of the FE model relies on creating the best possible discretization (mesh). A finer mesh generally provides more precise results by capturing stress gradients more effectively. Geometric characteristics with high-stress concentrations require a dense mesh to accurately predict the stress-strain behaviour. A mesh convergence study was performed to analyse the influence of mesh size on the outputs of interest. The meta-scaffold design was meshed with a range (0.3 to 0.04 mm) of element sizes, with the resulting force-displacement curve as shown in Fig. 3b.

The results indicated that there was no significant difference in the elastic range of the meta-scaffolds for element sizes below 0.1 mm. Hence, a 0.1 mm element size was considered sufficient to predict the stiffness and strength of the meta-scaffolds. As the study focused primarily on pre-yield behaviour, a final mesh size of 0.1 mm was chosen to model the meta-scaffold designs. This resulted in 2477,887 elements and 4635,536 nodes, with a solution time of 10,356.7 s. The negative Poisson's ratio was calculated as the numerically evaluated average lateral strain divided by the longitudinal strain.

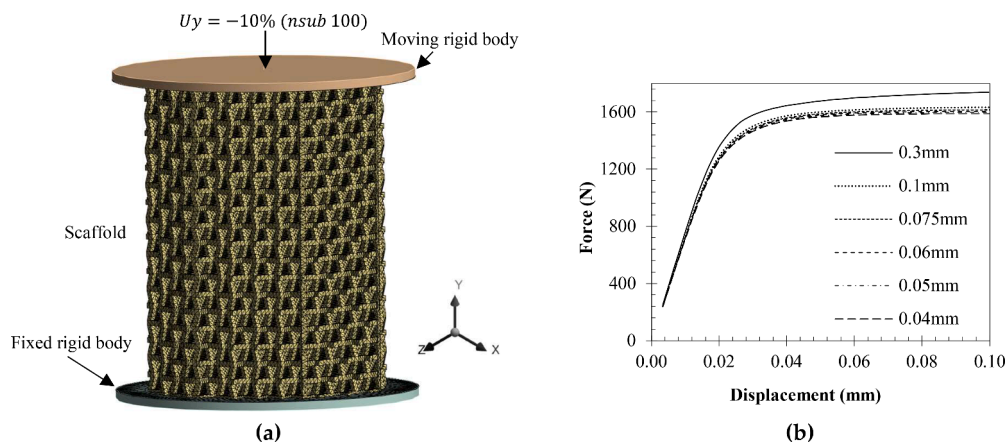


Fig. 3. Finite element model of the porous biomaterial showing (a) the boundary conditions and (b) the influence of mesh size on the resulting force-displacement characteristics.

2.4. Development of the proxy-model

Managing and controlling the contribution of all variables and their impact on meta-scaffold design pose challenges. Hence, the variables t_s and θ_s were selected for investigating their significance in both the $-v$ and mechanical performance of the meta-scaffold. Four responses (Poisson’s ratio, porosity, yield strength, and elastic modulus) were used to represent the model in this study. Through the proxy-model, the meta-scaffold’s performance can be predicted, revealing the design parameters with the most significant influence. The predictions were obtained by fitting simulation data to suitable polynomial equations derived from randomised experimental sets. Since there is no universal bone scaffold suitable for all patients, developing an optimised scaffold with high $-v$ allows to maximise internal stimulation for bone regeneration.

The proxy-model was developed using a combination of numerical and statistical methods to establish the relationship between design parameters and performance measures of the meta-scaffold. The central composite design (CCD) response surface methodology was used to form the training matrix for the proxy-model [63,64], as it offers high efficiency in sampling and leads to accurate response surface models with fewer experiments. All the different steps involved in the development of the proxy-model are summarised in Fig. 4.

For the proxy-model, the relationship between the output responses (y) and design changes (x) can be expressed using Eq. (1):

$$y = f(x_1, x_2, \dots, x_n) + \epsilon \tag{1}$$

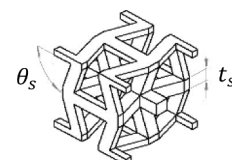
where n and ϵ represents the variables and error connected to output y . Where a 2nd order response surface is informing the proxy-model, y can be expressed using Eq. (2):

$$y = \beta_0 + \sum_{i=1}^k \beta_i x_i + \sum_{i=1}^k \beta_{ii} x_i^2 + \sum_i \sum_j \beta_{ij} x_i x_j + \epsilon \tag{2}$$

where $\beta_0, \beta_i, \beta_{ij}$ and β_{ii} are the regression coefficients that links the association between predictor variables and the response. Subsequently, these beta values are employed in the proxy-model to foretell the values of x corresponding to a specific response. Through conducting parametric analysis, the effects of t_s and θ_s on v, φ, σ_y and E can be determined. After the completion of the parametric analysis, the proxy-model can be used to optimise the meta-scaffold architecture to fulfil a designated multi-objective personalisation criterion.

Proxy-models find common application in cases where the number of input parameters affects the quality or performance of a design [64,65]. For this proxy-model, t_s and θ_s are the parametric variables of interest due to their impact on both $-v$ and the mechanical performance of the meta-scaffold. Table 3 illustrates how these variables correspond to the meta-scaffold, with t_s chosen to achieve a balance between porosity and

Table 3
Variables associated with the porous architecture informing the proxy-model training matrix.

	Variable	θ_s (deg.)	t_s (mm)
	-1	65	0.25
	0	70	0.30
	1	75	0.35

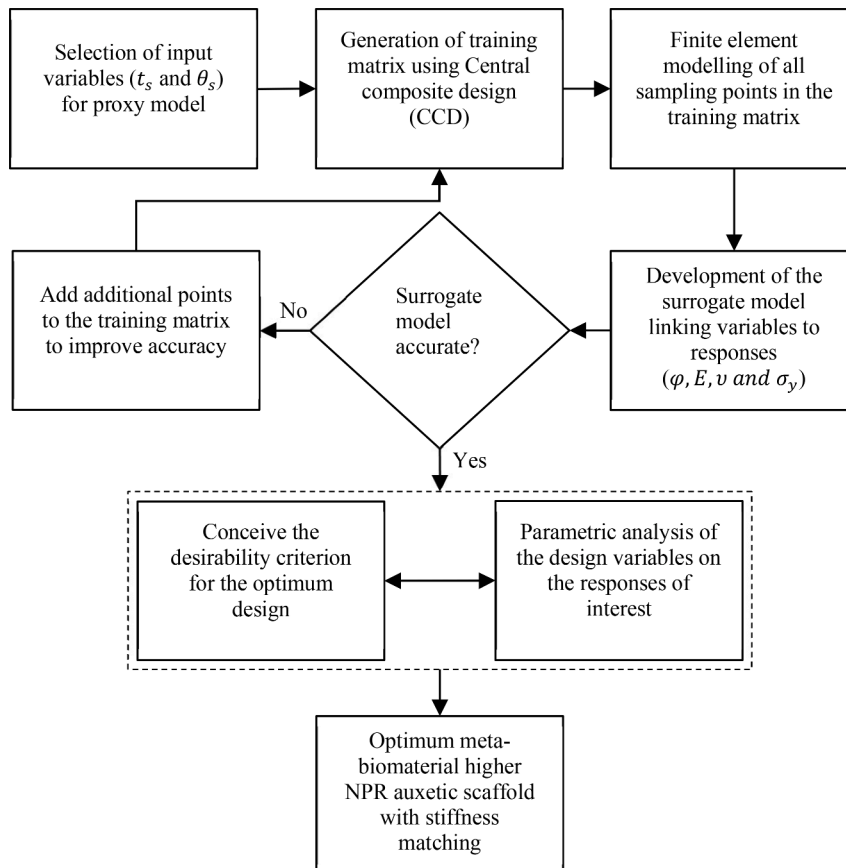


Fig. 4. The different steps involved in conceiving and generating the proxy-model for the patient-specific bone scaffold.

its ability to deform under load. θ_s ranges from 65° to 75° , with the lower limit representing the highest feasible angle that does not penetrate the struts. The upper limit is set at 75° to prevent +ve ν behaviour under compression.

2.5. Patient-specific formulation

The patient-specific personalisation is structured based on the proxy-model, allowing for the identification of a personalised solution that meets the specified requirements. The criteria can be established by integrating various performance objectives related to the design variables as illustrated by Eq. (3):

$$\begin{cases} \text{Minimise } f(x) = [f_1(x), f_2(x), \dots, f_i(x)] \\ \text{s.t. } x^l \leq x \leq x^u \end{cases} \quad (3)$$

where x^l signifies the lower bounds and x^u signifies the upper bounds of the variable parameters associated with the personalisation function $f(x)$. To devise a personalised high - ν , stiffness-matched tibial meta-scaffold, it is crucial to acquire the intended responses as outlined in Table 4. These represent the essential design parameters needed to achieve the highest lateral strain and maximum - ν , superior strength, and a targeted elastic modulus of 18 GPa [66] that corresponds to cortical tibial bone.

2.6. Meta-scaffold destructive testing

The materials testing apparatus utilized in this study was the Zwick 1474, which possessed a maximum load capacity of 100 kN. Uniaxial tension and compression experiments were performed on the CoCrMo bulk material and bone scaffold, respectively, employing this equipment. The experimental configuration included the incorporation of a mounted camera to record the deformation process, as visually depicted in Fig. 5. Conforming to the BSEN ISO 7500-1 [67] standard, the tests were conducted to explore the compressive behaviour of the meta-scaffolds. For statistical robustness, three samples from the same batch were carefully selected for the analysis. The test samples underwent loading at a controlled rate of 0.08 mm/s until failure.

3. Results and discussion

3.1. Meta-scaffold print quality

The SEM examination informed by Fig. 6 explored the difference in porosity between the ideal and l-PBF meta-scaffolds. The data shows that the use of shotblasting to post-process the printed meta-scaffolds have been effective with most of the semi-molten and loose powder particles completely removed. However, closer scrutiny of the meta-scaffold joints as highlighted by 'a' and 'b' indicates splatter contamination and fused adjacent particles affecting the joint quality of the meta-scaffold. Considering the complexity of the meta-scaffold architecture and the number of joints present, this can contribute to a reduction in porosity. This observation aligns with prior investigations [68], underscoring the importance of meticulously examining joint

Table 4

Personalisation scenario used to develop high - ν , patient-specific porous meta-scaffold.

Personalisation parameters	Expectation	Explanation
Negative Poisson's ratio ($-\nu$)	Maximise	Highest elastic strain
Elastic modulus (E)	18 GPa	Targeted stiffness matching
Yield strength (σ_y)	Maximise	High strength
Porosity (φ)	Maximise	High porosity

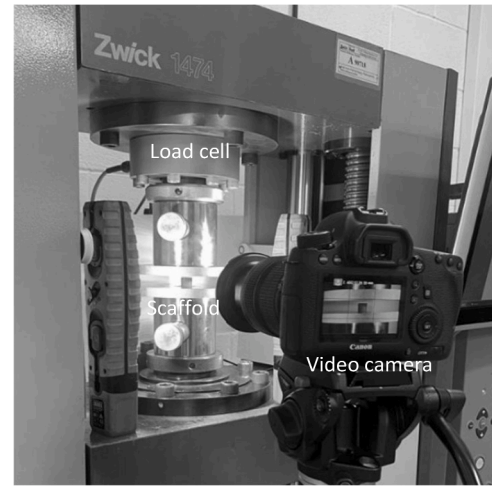


Fig. 5. Destructive material testing of the bulk material and meta-scaffold prototypes.

regions in 3D-printed meta-scaffolds. Furthermore, it also highlights the need to consider the tolerance aspects of l-PBF when conceiving porous architecture at the micron scale.

The post-shot blasted surface of the l-PBF meta-scaffolds displayed a surface finish of $3\text{--}5\ \mu\text{m Ra}$ (average roughness), this roughness could be advantageous for bone regeneration, as it provides a favourable environment for bone cells to grip into the meta-scaffold's pores. This feature might enhance the meta-scaffold's integration with surrounding bone tissue and promote better bone healing. While the interconnected porosity and representative geometry of the fabricated meta-scaffolds closely matched the intended CAD (Computer-Aided Design) geometry, there was some variation in the average strut thickness (Fig. 6). This variation, observed to be approximately $50\ \mu\text{m}$, has been documented in existing literature on l-PBF of thin struts ($<300\ \mu\text{m}$) [69–72]. The cumulative effect of this strut thickness variation resulted in an overall porosity reduction of roughly 9.69% compared to the ideal meta-scaffold design as summarised in Table 5. Overall, the meta-scaffolds exhibited a rough surface finish, potentially favourable for bone regeneration, while shot blasting proved effective in reducing the presence of semi-molten and loose powder particles. The variation in strut thickness, as well as the presence of joint regions, influenced the final porosity of the meta-scaffolds.

3.2. Finite element analysis

3.2.1. Verification of accuracy

The stress-strain behaviour of the 3D printed meta-scaffold was analysed both experimentally and numerically. Fig. 7. reveals that the numerical results closely mirror the elastic behaviour of the meta-scaffolds, indicating its capability to predict the mechanical response accurately. To characterise the validity of the numerical model, Table 6 compares key material parameters between numerical and physical test data namely the elastic modulus (E), yield stress (σ_y), and Poisson's ratio ($-\nu$) of the meta-scaffold. The comparison reveals a consistent trend between the two methods, with differences of 1.19%, 4.05% and 2.127% for E , σ_y and $-\nu$ respectively. Notably, Poisson's ratio remains negative, signifying auxetic behaviour in both numerical and physical test cases.

Overall, the stress-strain data indicates that the numerical model accurately predicts key mechanical parameters with an accuracy of 96.43%. The slight discrepancies observed between the numerical model and physical test data can be attributed to dimensional deviations during 3D printing as revealed in Fig. 6. Previous studies [73–78] have documented variations in geometry due to the stair-step effect and partly fused powder on the surface, which become increasingly

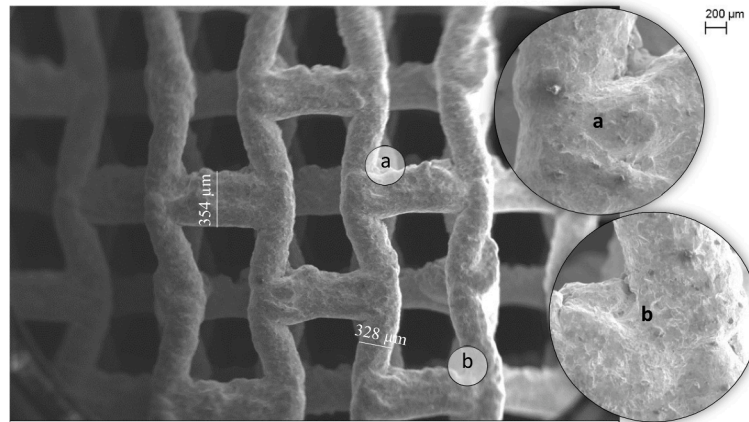


Fig. 6. Meta-scaffold morphology showing effect of L-PBF on wall thickness and variation of joints compared to the ideal. The highlighted sections indicated 'a' and 'b' reveal splatter contamination and accuracy of edges at strut joints.

Table 5
Change in porosity observed between L-PBF meta-scaffolds and their ideal CAD counterpart.

Properties	Patient-specific meta-scaffold		
	Ideal	L-PBF	% Difference
Porosity (%)	80.49	73.05	9.69

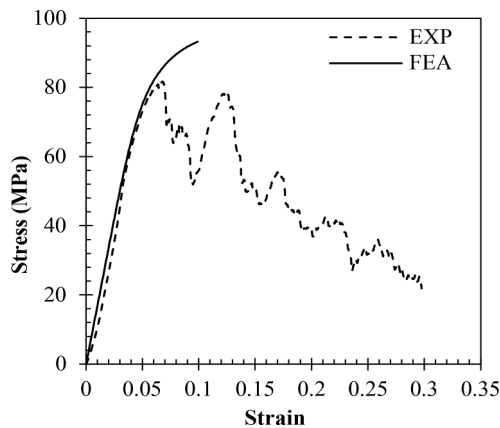


Fig. 7. Comparison between the stress-strain curves informed by numerical model and destructive tests.

Table 6
Difference between the numerical and physical test data.

Properties	EXP	FEA	% Difference
E (GPa)	1.66	1.68	1.19
σ_y (MPa)	71	74	4.05
ν	-0.240	-0.235	2.13

significant for porous and geometrically complex thin-walled structures like those studied here. While experimental data considers all irregularities, numerical models assume an idealised, homogeneous structure based on CAD designs, free from surface irregularities. Despite these challenges, the comparison of test data demonstrates reasonable agreement, indicating that the numerical meta-scaffold model can be used for parametric analysis.

3.2.2. Stress distribution in the meta-scaffold

During elastic compression of meta-scaffolds, macroscopic stresses generated within the material are proportional to the resulting strain (ϵ). Fig. 8 shows that the meta-scaffold experiences low stresses due to higher ϵ and Poisson's ratio ($-\nu$). For the auxetic meta-scaffold under examination, stress concentrations were notably observed at the joints, while stress distribution throughout the meta-scaffold volume appeared to be relatively uniform. Stress concentrations at joint regions are common in meta-scaffold structures, particularly those with complex geometries or irregular unit cells. These regions often serve as focal points for mechanical failure, where localised stresses can exceed the material's yield strength, leading to structural damage or collapse.

The geometry of the unit cell plays a pivotal role in determining how stress is distributed within the meta-scaffold structure, and gaining deeper insights into this distribution is essential for developing effective design guidelines. In cellular structures, stress concentration induced by geometry has a more significant impact on mechanical behaviour and failure than relative density alone [79]. Salimon et al. [80] attempted to establish relationships between stress (σ_y) and relative density (ρ_r) for cellular structures revealing that the inconsistencies between theoretical and experimental results were largely driven by stress concentration effects. However, literature [81–83] have also shown that certain meta-scaffold designs are more susceptible to stress concentration leading to premature failure. Nevertheless, the precise correlation between stress concentration and auxetic bone meta-scaffolds, remains an area yet to be explored.

3.3. Proxy-model for personalised response

3.3.1. Training matrix and regression analysis

Using a training matrix and regression analysis, a proxy-model was developed linking the geometrical inputs t_s and θ_s to the desired outputs for ν , ϕ , σ_y and E . A total of 13 training experiments were conceived featuring two input design as shown in Table 7. Meta-scaffold designs were generated for each training experiment case featuring the respective input parameters and evaluated for the four output responses with results as summarised in Table 7. This approach enables exploration of a wide range of variables and their interrelationships, significantly influencing meta-scaffold properties. The training matrix is used to inform proxy-model for the meta-scaffold that enables accurate prediction of mechanical properties.

Subsequently, best-fit indicators for the results were calculated. Linear models were found to effectively characterise ϕ , ν and E as listed in Eqs. (4), (5), and (6), respectively. However, σ_y exhibited a quadratic trend, indicating interaction effects amongst input parameters as expressed in Eq. (7):

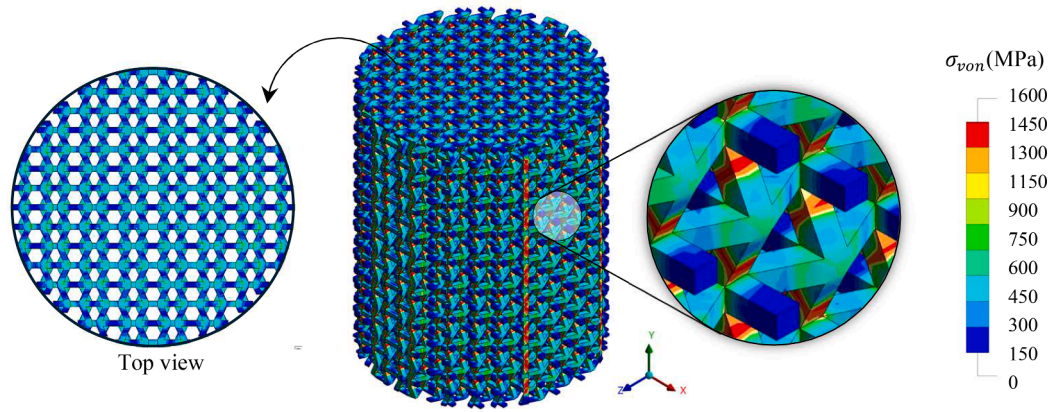


Fig. 8. Numerical evaluation reveals stress distribution in the auxetic meta-scaffold under axial compression, illustrating uniform stress distribution along the top surface and variations in stress levels across the unit cell cross-section. The von Mises scale indicate areas of high stress as potential failure locations when safe load is exceeded.

Table 7

Input and output parameters informing the training matrix for personalised meta-scaffold.

Training experiment	Input		Output			
	t_s (mm)	θ_s (Deg.)	ν	φ (%)	σ_y (MPa)	E (GPa)
1	0.30	70	-0.27	79.75	46	14.89
2	0.34	66	-0.21	73.95	60	19.08
3	0.30	70	-0.27	79.75	46	14.89
4	0.26	66	-0.38	83.77	30	08.60
5	0.34	74	-0.16	75.50	80	22.58
6	0.30	65	-0.28	78.93	44	12.91
7	0.30	75	-0.22	80.43	52	16.79
8	0.30	70	-0.27	79.75	46	14.89
9	0.30	70	-0.27	79.75	46	14.89
10	0.35	70	-0.19	73.46	76	22.6
11	0.30	70	-0.27	79.75	46	14.89
12	0.26	74	-0.31	84.71	38	11.48
13	0.25	70	-0.37	85.36	32	08.94

$$\varphi = 106.23 - 126.78t + 0.16\theta \quad (4)$$

$$\nu = -1.38 - 2.03t + 7.24e^{-3}\theta \quad (5)$$

$$E = -57.56 + 144.59t + 0.42\theta \quad (6)$$

$$\sigma_y = 1106.34 - 3245.44t - 19.81\theta + 24t\theta + 3400t^2 + 0.1\theta^2 \quad (7)$$

3.3.2. Accuracy of the proxy-model

Prior to employing the proxy-models for parametric analysis, analysis of variance (ANOVA) was conducted to ascertain their accuracy [84–86]. The proxy models were used to explore the correlation between design inputs and the output performance of the auxetic bone meta-scaffold. Table 8 provides a summary of the adequacy measures

Table 8

ANOVA signifying the accuracy of the proxy-model developed for personalised ν bone meta-scaffold.

Model	F-value	p-value	Statistical measurements			
			R^2	Adj- R^2	Pre- R^2	Adeq-precision
φ	844.03	< 0.0001	0.9941	0.9929	0.9877	84.8287
E	466.58	< 0.0001	0.9894	0.9873	0.9786	61.0712
ν	131.63	< 0.0001	0.9634	0.9561	0.9202	31.8144
σ_y	74.97	< 0.0001	0.9817	0.9686	0.8696	26.4704

used to evaluate the quality of the proxy model. Substantial F-values and low p-values were observed for all the four proxy-models, indicating their statistical significance. P-values below 0.05 suggest significant model terms. Notably, the p-values for all generated models (Eqs. (4)–(7)) are below 0.0001 signifying high accuracy [87].

Furthermore, all models demonstrate an adequate precision ratio exceeding 4, indicating minimal noise in the model [52,87–91]. Additionally, high R^2 values (>0.9) across all models suggest favourable agreement for the proxy-model. The ANOVA analysis confirms the accuracy of all four proxy-models, enabling parametric analysis within the considered range of design variables. After the ANOVA assessment, the relationship between finite element and proxy-model predictions was examined (Fig. 9). Notably, for all evaluated responses (φ , E , ν and σ_y), the predictions of the proxy-model closely aligned with numerical results represented by the diagonal dotted line. Expanding on these findings, it is essential to acknowledge the significance of accurate proxy-models in informing material design and engineering processes. By providing insights into the complex relationships between geometric parameters and material properties, the proxy-model developed here facilitate optimisation of the meta-scaffold for personalised performance.

3.4. Meta-scaffold performance

3.4.1. Porosity

Analysis of the data in Fig. 10 highlights the significant impact of strut thickness on porosity, as evidenced by the gradient of the slope in Fig. 10a, followed by the influence of the strut angle (Fig. 10b). The linear increase in porosity with decreasing strut thickness reveals a direct correlation between the two parameters. A comparable trend is observed for strut angle albeit with a shallower linear slope, indicating its lesser but still notable influence on porosity. This is because as strut thickness decreases, the relative density of the meta-scaffold diminishes. Thinner struts occupy less volume within the structure while still providing structural support.

This reduction in volume occupied by the struts allows for more space between them, consequently increasing the overall porosity of the meta-scaffold. The linear relationship between decreasing strut thickness and increasing porosity is thus expected, reflecting the direct impact of this parameter on the structural composition of the meta-scaffold. Similarly, the strut angle influences the length and orientation of the struts within the meta-scaffold. Increasing angle leads to a reduction in the effective length of the struts due to the re-entrant architecture, whereby the struts curve inward. This reduction in strut length effectively increases the gaps or void spaces within the meta-scaffold, promoting greater porosity. Insight into the combined impact

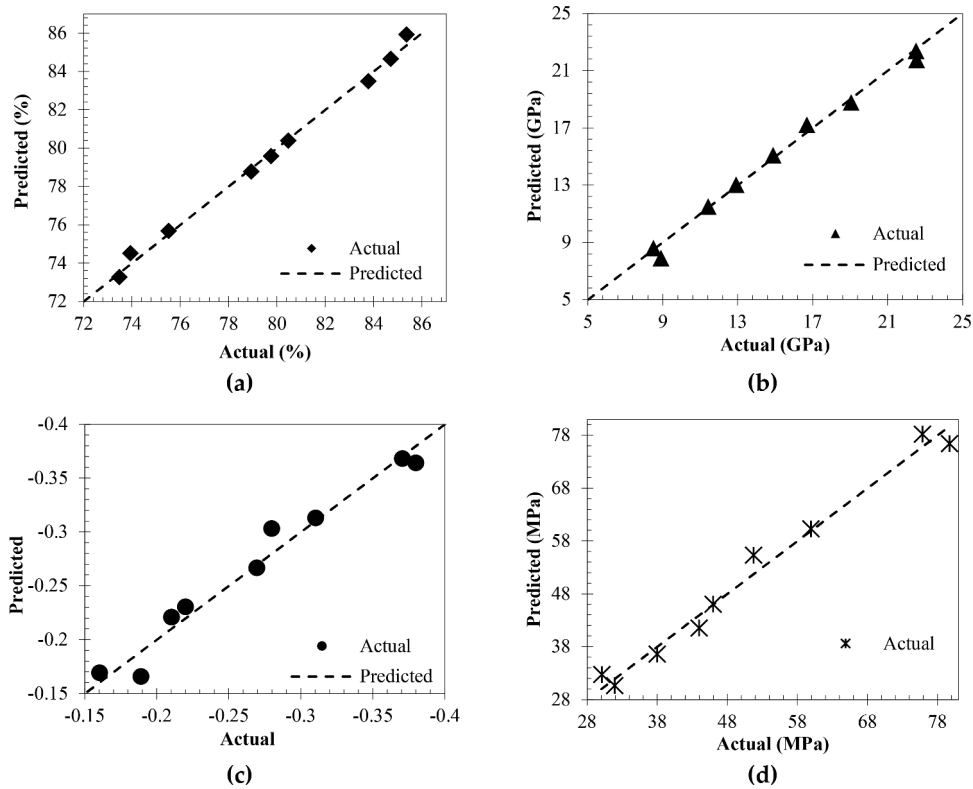


Fig. 9. Evaluating the accuracy of the proxy-model prediction (diagonal dotted line) with that of finite element results (point cloud) for the meta-scaffold showing (a) porosity, (b) elastic modulus, (c) negative Poisson's ratio and (d) yield strength.

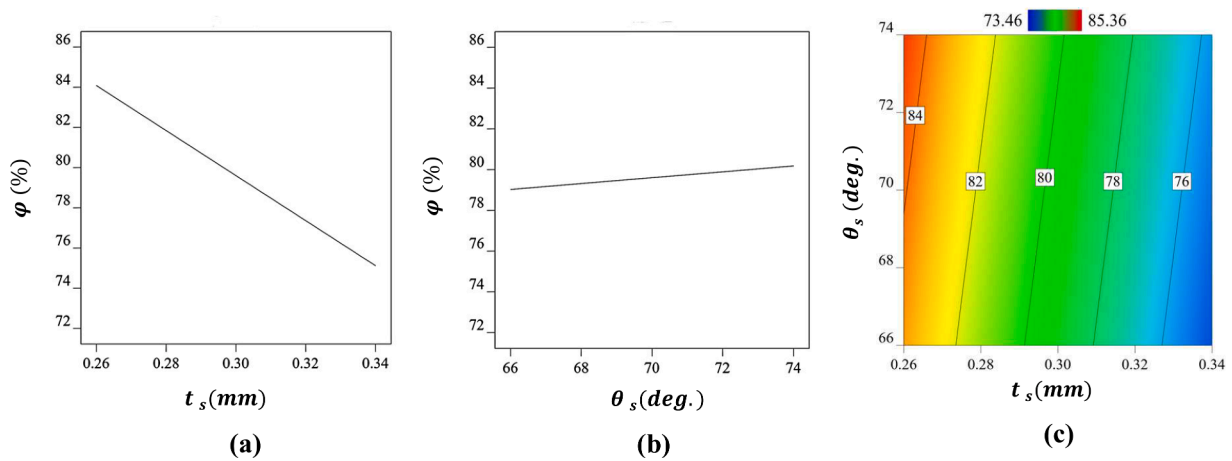


Fig. 10. The impact of geometrical variables on meta-scaffold performance showing (a) the effect of strut thickness on porosity, (b) strut angle on porosity, and (c) the mutual reliance of strut thickness and angle on porosity.

of strut thickness and angle on porosity can be found in Fig. 10c. Porosity seems to be primarily relying on t_s , with θ_s playing a secondary role in determining meta-scaffold porosity. Decreasing t_s and increasing θ_s lead to a linear rise in porosity, peaking at 85.36% for the lowest t_s and highest θ_s configurations. This suggests that thinner struts diminish the structure's relative density, thereby elevating porosity, while increasing angle reduces strut length, similarly enhancing porosity.

Considering the interplay between design inputs, the lowest porosity (73.46%) occurs at the highest t_s and lowest θ_s values, with the converse yielding the highest porosity. Although the interaction effect between t_s and θ_s influences porosity, its cumulative impact appears moderate, as depicted in Fig. 10c. Consequently, porosity modulation primarily hinges on varying t_s . The preeminent influence of thickness underscores

its pivotal role in dictating porosity within the meta-scaffold. Overall, the first-order effects of t_s is the most significant parameter on porosity for the meta-scaffold. This suggests that reducing t_s yields higher porosity compared to a similar increment in θ_s .

3.4.2. Elastic modulus

Fig. 11 shows that the elastic modulus of the meta-scaffold is primarily dependant on the thickness parameter (Fig. 11a) and slightly on angle (Fig. 11b) linearly. Elastic modulus increases consistently with the rise in t_s and θ_s , leading to the highest value of 22.6 GPa at their maximum, as shown in Fig. 11c. The reason for the significant influence of t_s on the elastic modulus of the meta-scaffold lies in its direct impact on the structural integrity and material density. When the thickness

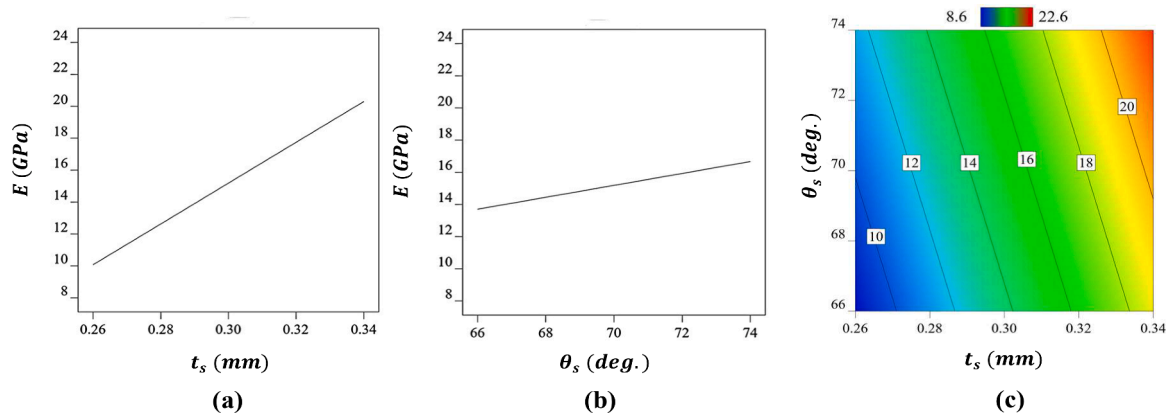


Fig. 11. The impact of geometrical variables on meta-scaffold performance showing (a) the effect of strut thickness on elastic modulus, (b) strut angle on elastic modulus, and (c) the mutual reliance of strut thickness and angle on elastic modulus.

increases, it results in a denser structure with more material to resist deformation and distribute loads. This increased density leads to higher stiffness and, consequently, a higher elastic modulus.

On the other hand, while θ_s also plays a role in influencing E , its effect is somewhat secondary. The angle affects the spacing and arrangement of the structural elements within the scaffold. A higher θ_s helps to spread the beams further apart, which can reduce the likelihood of buckling and enhance the elastic modulus by allowing for better load distribution. However, this effect is typically not as pronounced as the impact of thickness. Therefore, due to its direct influence on material density and structural integrity, changes in t_s have a more significant and direct effect on the elastic modulus of the meta-scaffold compared to alterations in θ_s .

While t_s is the most significant design variable driving the stiffness of the meta-scaffold, θ_s can also be seen to influence the performance. This means modulating both thickness and angle can influence E at different rates. Fig. 11c shows that although there is a certain interdependence of the geometrical variables, E is still largely driven by t_s . As such, increasing t_s will yield a higher E in comparison to increasing the same amount of θ_s . Overall, the first-order effect of t_s is the most significant, followed by the θ_s on the stiffness of meta-scaffold.

3.4.3. Negative Poisson's ratio

The negative Poisson's ratio of the meta-biomaterial is observed to be contingent upon both t_s and θ_s , as evidenced in Fig. 12, indicating a variation in lateral strain based on the values of these design parameters.

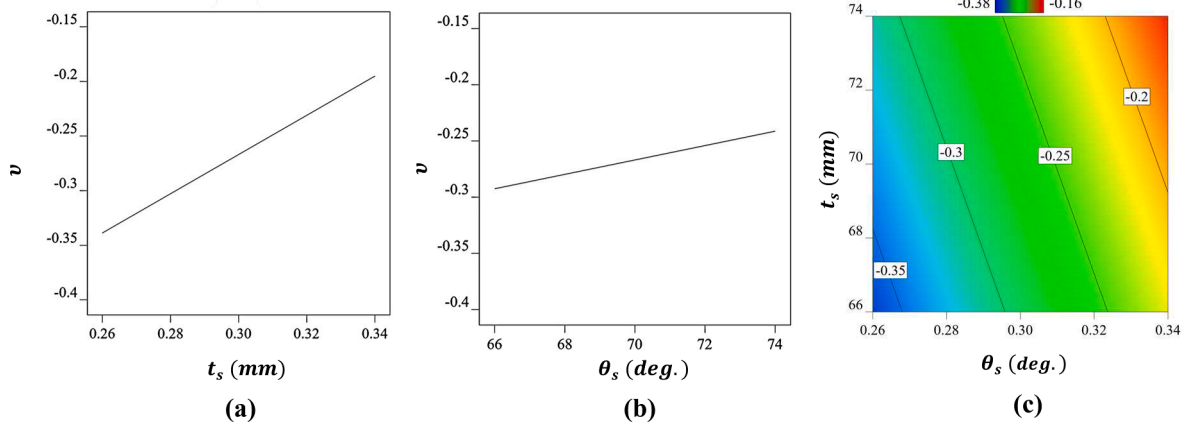


Fig. 12. The impact of geometrical variables on meta-scaffold performance showing (a) the effect of strut thickness on Poisson's ratio, (b) strut angle on Poisson's ratio, and (c) the mutual reliance of strut thickness and angle on Poisson's ratio.

$-\nu$ demonstrates a linear increase, albeit at a slower pace, in correlation with t_s (Fig. 12a), compared to the reduction in θ_s (Fig. 12b), as indicated by the distinct slopes of the linear trend. The lowest angle and thickness correspond to the highest $-\nu$ value, as shown in Fig. 13c. The reason behind the significant influence of t_s and θ_s on the negative Poisson's ratio of the meta-scaffold lies in their effects on the material's structural arrangement and behaviour under loading conditions.

Firstly, t_s influences $-\nu$ by affecting the relative density and porosity of the meta-biomaterial. As t_s decreases, the relative density decreases while porosity increases. This change in density and porosity alters the scaffold's ability to deform laterally when subjected to axial loads, thereby affecting its negative Poisson's ratio. Lower thickness allows for more lateral deformation, leading to higher $-\nu$ values. Secondly, θ_s impacts $-\nu$ by influencing the distribution of the axial load within the material. Larger angles result in more material being influenced by the axial load, which can lead to increased lateral strain and higher $-\nu$ values. Overall, the most influential factors determining $-\nu$ are the first-order effect of t_s followed by θ_s . Consequently, the $-\nu$ of the meta-biomaterial can be modulated by adjusting both thickness and angle to achieve the desired performance.

3.4.4. Yield strength

The yield strength of the meta-scaffold is predominantly influenced by t_s with a minor effect from θ_s , as shown in Fig. 13a and 13b, respectively. This observation arises from the significant impact of porosity on material deformation. As thickness increases, the relative density also

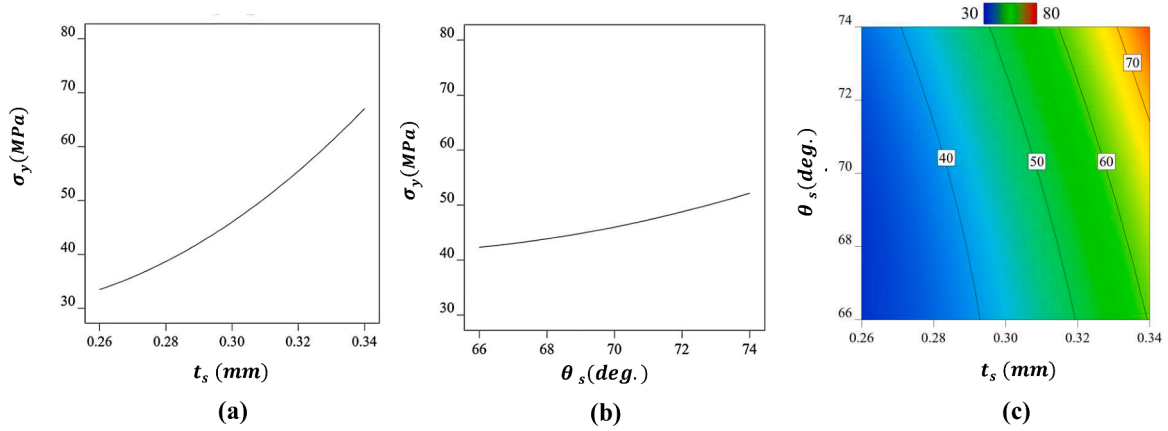


Fig. 13. The impact of geometrical variables on meta-scaffold performance showing (a) the effect of strut thickness on yield strength, (b) strut angle on yield strength, and (c) the mutual reliance of strut thickness and angle on yield strength.

risers, resulting in higher strength due to increased material resistance against plastic deformation. Both thickness and angle exhibit a quadratic relationship with σ_y , demonstrating a consistent increase in yield strength as both parameters rise. Fig. 13c indicates a notable interaction effect between the design parameters, showcasing the highest yield strength when both t_s and θ_s reach their peaks. The order of influence on the yield strength of the meta-biomaterial is primarily $t_s > \theta_s > t_s \theta_s$.

The quadratic relationship observed for both thickness and angle indicates that the yield strength increases consistently with increases in these parameters, but the rate of increase may vary. Moreover, the interaction effect between thickness and angle suggests that their combined influence on yield strength is significant, with the highest yield strength achieved when both parameters are optimised. The diverse effects of design variables on porosity and mechanical performance underscore the potential for tailored performance through parameter modulation.

Materials with high negative Poisson's ratio hold promise for load-bearing tissue engineering scaffolds. Such architectures exhibit localised shrinking under axial loads and demonstrate arch-shaped bending behaviour, effectively resisting bending deformation while maintaining compatibility with the host bone. Literature shown that this kind of material possesses many advantages compared to conventional counterparts [92]. Furthermore, other physical properties including hardness [93], shear resistance [94] and energy absorption [95] are improved. Although not directly targeting bone scaffolds, increasing number of materials with negative Poisson's ratio are being investigated for numerous applications.

3.5. Performance personalisation

When there is a need to conceive multiple performance targets, the adoption of a multi-dimensional decision-making methodology becomes imperative [96]. This approach builds upon the proxy-model established for the relevant performance parameters to discern an optimal solution satisfying various desirability criteria [97–99]. The ideal meta-scaffold should fulfil several personalised performance criteria, including maximizing $-v$ to achieve micro-strain stimulation, achieving a stiffness of 18 GPa akin to adult cortical bone to avert stress shielding and maladapted stress concentration, and maximizing yield strength while upholding high porosity for optimal compressive strength and bone reintegration support. Consequently, the meta-scaffold performance personalisation problem can be formulated using Eq. (8):

$$\left\{ \begin{array}{l} \text{Maximise } \sigma_y = f_1(\theta_s, t_s) \\ \text{Maximise } \varphi = f_2(\theta_s, t_s) \\ \text{Maximise } -v = f_3(\theta_s, t_s) \\ \text{s.t } E = 18 \text{ GPa} \\ \\ \text{s.t } 65.0 \leq \theta_s \leq 75.0 \\ \text{s.t } 0.25 \leq t_s \leq 0.35 \end{array} \right. \quad (8)$$

The process of multi-dimensional decision-making often involves dealing with multiple responses, resulting in the generation of numerous solutions. To consolidate these solutions into a unified objective, a desirability function is employed, denoted as D , which aligns with the desirable range for each response (d_i). The desirability approach is a widely adopted strategy to tackle such complexities. It operates under the assumption that the desired outcome encompasses multiple favourable characteristics, and any solution deviating from these desired limits is considered unacceptable. The desirability method facilitates the representation of the least and most desirable outcomes within the range of 0 to 1. When there are n responses, the multi-dimensional decision-making function is expressed as the geometric mean of all transformed responses, as outlined in Eq. (9):

$$D = (d_1 \cdot d_2 \cdot \dots \cdot d_n)^{\frac{1}{n}} = \left(\prod_{i=1}^n d_i \right)^{\frac{1}{n}} \quad (9)$$

Fig. 14 illustrates the solution to the meta-scaffold personalisation criterion, showcasing the desirability objective concerning the strut angle and thickness of the meta-scaffold. At the specific values detailed in Table 9, the desirability reached its maximum achievable value of 1. This means that a meta-scaffold featuring the design parameters summarised in Table 9 can achieve the performance personalisation target conceived by Eq. (8).

The multi-dimensional decision-making solution presented in Fig. 14 reveals the essential design parameters necessary for fabricating the personalised meta-scaffolds. Table 9 outlines the predicted optimal solution for the meta-biomaterial, meeting all desirability criteria, including stiffness matching to host tibial bone and a high negative Poisson's ratio to maximise micro-strain effect. Fig. 14 indicate that the highest desirability score correlates closely with the lowest strut angle and the highest strut thickness of the meta-scaffold. In order to confirm

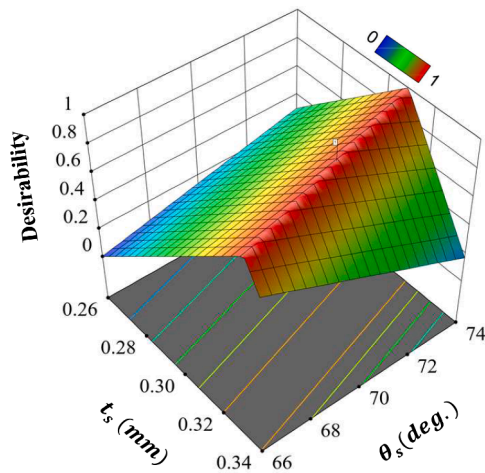


Fig. 14. Outcome of the multi-dimensional decision-making solution showing the design parameters required to create the personalised meta-scaffold.

Table 9

Predicted design parameters to create the personalised meta-scaffold with all desirable functionalities.

Number	t_s (mm)	θ_s (Deg.)	Desirability
1	0.325	67.93	1

the personalised performance, the meta-scaffold design featuring the optimum design parameters was generated and characterised as with results summarised in Fig. 15. The resulting stress profile according to von-Mises criteria highlights a stronger meta-scaffold exhibiting the desired characteristics, as summarized in Table 10. A detailed comparison between the proxy-model and FE predictions of the personalised meta-scaffold is provided in the same table.

Comparing the results predicted between the two methodologies (Table 10) it can be seen that the proxy-model slightly overestimated the Poisson’s ratio, yield strength, and elastic modulus by 3.04%, 2.37%, and 2.61%, respectively, while underestimating the porosity by 0.4%. Nonetheless, the results indicate that the optimal design offers a meta-scaffold with desirable characteristics, ensuring high Poisson’s ratio performance and stiffness matching behaviour. Consequently, the optimum meta-biomaterial presents a promising solution for bone scaffold applications where high Poisson’s ratio and stiffness matching to host bone are essential. The outcomes of this investigation confirm the precision of the proxy-model in evaluating the mechanical behaviour of the re-entrant meta-scaffold at an accuracy of 96.9%. This offers significant

Table 10

Performance of the personalised meta-scaffold predicted by the proxy and numerical models.

Item	ν	φ	E	σ_y
Predicted	-0.230	76.042	18.00	58.59
FEM	-0.223	76.351	17.53	57.20
% Difference	3.04	0.40	2.61	2.37

potential for developing meta-scaffolds with personalised functionalities to suite a range of targeted performances. These findings offer valuable insights for the personalised reconstruction of critical-size defects with tailored mechanical responses.

3.6. Future prospects

Co-Cr alloys have a higher elastic modulus, density, and stiffness compared to bone, resulting in greater stress shielding than Ti and Ti alloys. The excessive structural stiffness of Co-Cr alloy can be addressed through 3D printing. By integrating nano- and micro-geometry into the alloy, it is plausible to decrease the elastic modulus and minimize the stiffness discrepancy between the alloy and bone. The proxy-model developed in this study offers a methodology for developing precision-driven design and fabrication of load-bearing stiffness matched meta-scaffolds. Personalised mechanical performance of meta-scaffolds can lead to more effective reconstruction of load bearing critical size bone defects, resulting in better clinical outcomes.

The opportunity to utilise topology optimisation [100] techniques in meta-scaffold design is compelling. Whilst well-established in mechanical structure optimisation, extending this methodology to meta-scaffolds offers compelling prospects. The intricate geometries and material compositions inherent in meta-scaffolds necessitate tailored optimisation strategies. Future programs will investigate the potential of topology optimisation in enhancing meta-scaffold design, considering mechanical performance alongside critical parameters such as biocompatibility and manufacturability. Integration of these methodologies may yield meta-scaffolds with superior mechanical properties, enriching their functionality for biomedical applications.

3.7. Potential challenges for commercialisation

The presented architecture and more generally the commercialisation of l-PBF for personalised load-bearing architectures for critical size tibial reconstruction faces several challenges. The primary concern is the need for precise control over the manufacturing process to ensure the reproducibility and reliability of the implants. This involves optimising parameters such as laser power, scanning speed, and powder quality to achieve desired mechanical properties and dimensional accuracy.

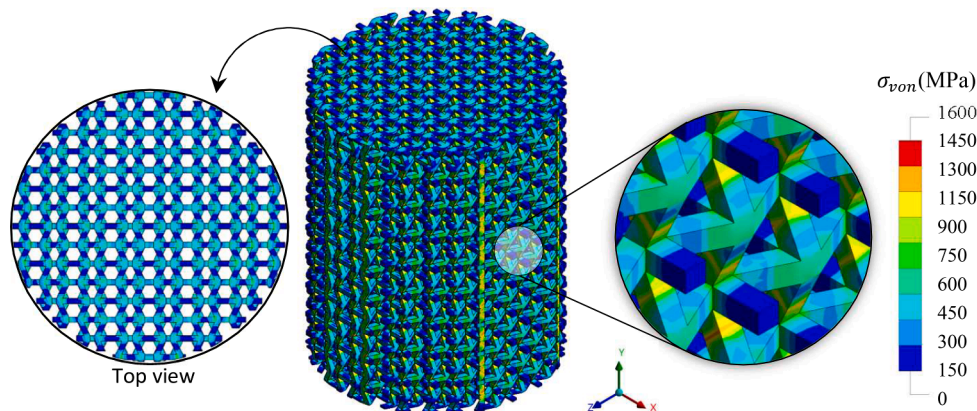


Fig. 15. Stress distribution of the stiffness matched personalised meta-scaffold identified by the proxy-model.

Given the critical nature of load-bearing implants, stringent regulatory requirements must also be met to ensure patient safety and efficacy. This involves comprehensive testing to demonstrate the biocompatibility, mechanical strength, and long-term durability of the implants. The scalability and cost-effectiveness are also significant considerations. While l-PBF offers the advantage of producing complex geometries with excellent material properties, the high initial capital investment and operational costs may limit its widespread adoption for personalised implants. Streamlining production processes and optimising material usage are essential to make personalised tibial reconstruction economically viable.

Addressing these challenges will require collaboration between researchers, clinicians, regulatory bodies, and industry partners to advance l-PBF technology, establish standardised protocols, and navigate regulatory pathways. Despite the hurdles, the potential benefits of personalized load-bearing implants for tibial reconstruction, including improved patient outcomes and reduced risk of complications, make this endeavour worth pursuing.

4. Conclusion

This study explored the transformative potential of CoCrMo superalloy and laser powder bed fusion additive manufacturing technique for the development of personalised meta-scaffolds signified by high negative Poisson's ratios. The methodology succeeded in crafting a CoCrMo meta-scaffold with precisely tuned negative Poisson's ratios and targeted elastic modulus matching the stiffness of an adult tibia. Revealing a proxy-model, the study characterised the impact of input design variables, including strut thickness (t_s) and angle (θ_s) on targeting performance parameters such as negative Poisson's ratio ($-v$), porosity (φ), strength (σ_y), and elastic modulus (E) specific to meta-scaffold. This methodological framework facilitated the creation of meta-scaffold tailored to withstand the rigors of load-bearing tibial reconstruction applications. The resultant meta-scaffold showcased a diverse spectrum of $-v$, φ , σ_y , and E spanning from -0.16 to -0.38 , 73.46–85.36%, 30–80 MPa, and 8.6–22.6 GPa, respectively. The multi-dimensional decision-making algorithm unveiled a personalised meta-scaffold offering a negative Poisson's ratio of 0.223 coupled with a targeted E of 17.53 GPa, while upholding strength and porosity of 57.2 MPa and 76.35%, respectively. Parametric analysis showed a linear correlation for Poisson's ratio, porosity and elastic modulus with strut thickness exerting a predominant influence over strut angle. However, yield strength demonstrated a quadratic association with the same design variables. When it comes to modulating meta-scaffold performance the primary influence was for strut thickness followed by angle in the order $t_s > \theta_s$, where their interplay proved consequential, particularly for σ_y .

Declaration of competing interest

All authors whose names are listed immediately below certify that they have NO affiliations with or involvement in any organisation or entity with any financial interest (such as honoraria; educational grants; participation in speakers' bureaus; membership, employment, consultancies, stock ownership, or other equity interest; and expert testimony or patent-licensing arrangements), or non-financial interest (such as personal or professional relationships, affiliations, knowledge or beliefs) in the subject matter or materials discussed in this manuscript.

References

- [1] Gupta K, Meena K. Artificial bone scaffolds and bone joints by additive manufacturing: a review. *Bioprinting* 2023;31:e00268. <https://doi.org/10.1016/j.bprint.2023.e00268>.
- [2] Jia Z, Xu X, Zhu D, Zheng Y. Design, printing, and engineering of regenerative biomaterials for personalized bone healthcare. *Prog Mater Sci* 2023;134:101072. <https://doi.org/10.1016/j.pmatsci.2023.101072>.
- [3] Vance A, Bari K, Arjunan A. Compressive performance of an arbitrary stiffness matched anatomical Ti64 implant manufactured using direct metal laser sintering. *Mater Des* 2018;160:1281–94. <https://doi.org/10.1016/j.matdes.2018.11.005>.
- [4] Vyavahare S, Mahesh V, Mahesh V, Harursampath D. Additively manufactured meta-biomaterials: a state-of-the-art review. *Compos Struct* 2023;305:116491. <https://doi.org/10.1016/j.compstruct.2022.116491>.
- [5] Arjunan A, Baroutaji A, Robinson J, Wang C. Tissue engineering concept. *Ref Modul Mater Sci Mater Eng* 2021. <https://doi.org/10.1016/B978-0-12-815732-9.00120-0>.
- [6] Kolken HMA, Garcia AF, Du Plessis A, Meynen A, Rans C, Scheys L, Mirzaali MJ, Zadpoor AA. Mechanisms of fatigue crack initiation and propagation in auxetic meta-biomaterials. *Acta Biomater* 2022;138:398–409. <https://doi.org/10.1016/j.actbio.2021.11.002>.
- [7] Shirzad M, Zolfagharian A, Bodaghi M, Nam SY. Auxetic metamaterials for bone-implanted medical devices: recent advances and new perspectives. *Eur J Mech - A/Solids*. 2023;98:104905. <https://doi.org/10.1016/j.euromechsol.2022.104905>.
- [8] Chen D, Li D, Pan K, Gao S, Wang B, Sun M, Zhao C, Liu X, Li N. Strength enhancement and modulus modulation in auxetic meta-biomaterials produced by selective laser melting. *Acta Biomater* 2022;153:596–613. <https://doi.org/10.1016/j.actbio.2022.09.045>.
- [9] Abdelaal O, Darwish S. Analysis, fabrication and a biomedical application of auxetic cellular structures. *Int J Eng Innov Technol* 2012;2:218–23.
- [10] K.B. Hazlehurst, The adoption of laser melting technology for the manufacture of functionally graded cobalt chrome alloy femoral stems, (2014).
- [11] Sumner DR, Galante JO. Determinants of stress shielding: design versus materials versus interface. *Clin Orthop Relat Res* 1992;202–12. <https://doi.org/10.1097/00003086-199201000-00020>.
- [12] Chao L, Jiao C, Liang H, Xie D, Shen L, Liu Z. Analysis of mechanical properties and permeability of trabecular-like porous scaffold by additive manufacturing. *Front Bioeng Biotechnol* 2021;9:1–13. <https://doi.org/10.3389/fbioe.2021.779854>.
- [13] Wanniarachchi CT, Arjunan A, Baroutaji A, Singh M. 3D printing customised stiffness-matched meta-biomaterial with near-zero auxeticity for load-bearing tissue repair. *Bioprinting* 2023;33:e00292. <https://doi.org/10.1016/j.bprint.2023.e00292>.
- [14] Arjunan A, Robinson J, Al Ani E, Heaselgrave W, Baroutaji A, Wang C. Mechanical performance of additively manufactured pure silver antibacterial bone scaffolds. *J Mech Behav Biomed Mater* 2020;112:104090. <https://doi.org/10.1016/j.jmbmm.2020.104090>.
- [15] Arjunan A, Robinson J, Baroutaji A, Tuñón-Molina A, Martí M, Serrano-Aroca Á. 3D printed cobalt-chromium-molybdenum porous superalloy with superior antiviral activity. *Int J Mol Sci* 2021;22. <https://doi.org/10.3390/ijms222312721>.
- [16] Arjunan A, Baroutaji A, Robinson J, Wang C. Antibacterial biomaterials in orthopedics. *Ref Modul Mater Sci Mater Eng* 2021. <https://doi.org/10.1016/B978-0-12-815732-9.00131-5>.
- [17] Li L, Shi J, Zhang K, Yang L, Yu F, Zhu L, Liang H, Wang X, Jiang Q. Early osteointegration evaluation of porous Ti6Al4V scaffolds designed based on triply periodic minimal surface models. *J Orthop Transl* 2019;19:94–105. <https://doi.org/10.1016/j.jot.2019.03.003>.
- [18] Zhang L, Song B, Choi SK, Shi Y. A topology strategy to reduce stress shielding of additively manufactured porous metallic biomaterials. *Int J Mech Sci* 2021;197:106331. <https://doi.org/10.1016/j.jimecs.2021.106331>.
- [19] Jiang Y, Li Y. 3D printed auxetic mechanical metamaterial with chiral cells and Re-entrant cores. *Sci Rep* 2018;8:2397. <https://doi.org/10.1038/s41598-018-20795-2>.
- [20] Park YJ, Kim JK. The effect of negative Poisson's ratio polyurethane scaffolds for articular cartilage tissue engineering applications. *Adv Mater Sci Eng* 2013;2013. <https://doi.org/10.1155/2013/853289>.
- [21] Arjunan A, Baroutaji A, Praveen AS, Robinson J, Wang C. Classification of biomaterial functionality. *Ref Modul Mater Sci Mater Eng* 2020. <https://doi.org/10.1016/B978-0-12-815732-9.00027-9>.
- [22] Choi HJ, Lee JJ, Park YJ, Shin J-WJWJW, Sung H-JJ, Shin J-WJWJW, Wu Y, Kim JK. MG-63 osteoblast-like cell proliferation on auxetic PLGA scaffold with mechanical stimulation for bone tissue regeneration. *Biomater Res* 2016;20:33. <https://doi.org/10.1186/s40824-016-0080-4>.
- [23] M. Ngiam, S. Liao, T. Ong Jun Jie, Xiaodi Sui, Yixiang Dong, S. Ramakrishna, C.K. Chan, Effects of mechanical stimulation in osteogenic differentiation of bone marrow-derived mesenchymal stem cells on aligned nanofibrous scaffolds; <http://dx.doi.org/10.1177/0883911510393162>. 26 (2010) 56–70. <https://doi.org/10.1177/0883911510393162>.
- [24] Praveen AS, Arjunan A, Baroutaji A. Coatings for dental applications. *Ref Modul Mater Sci Mater Eng* 2021. <https://doi.org/10.1016/B978-0-12-815732-9.00114-5>.
- [25] Kim Y, Son KH, Lee JW. Auxetic structures for tissue engineering scaffolds and biomedical devices. *Materials (Basel)* 2021;14. <https://doi.org/10.3390/ma14226821>.
- [26] Velasco MA, Narváez-Tovar CA, Garzón-Alvarado DA. Design, materials, and mechanobiology of biodegradable scaffolds for bone tissue engineering. *Biomed Res Int* 2015;2015. <https://doi.org/10.1155/2015/729076>.
- [27] Perier-Metz C, Duda GN, Checa S. Mechano-biological computer model of scaffold-supported bone regeneration: effect of bone graft and scaffold structure on large bone defect tissue patterning. *Front Bioeng Biotechnol* 2020;8:1–15. <https://doi.org/10.3389/fbioe.2020.585799>.

- [28] Milan JL, Planell JA, Lacroix D. Simulation of bone tissue formation within a porous scaffold under dynamic compression. *Biomech Model Mechanobiol* 2010; 9:583–96. <https://doi.org/10.1007/s10237-010-0199-5>.
- [29] Torres-Sanchez C, Al Mushref FRA, Norrito M, Yendall K, Liu Y, Conway PP. The effect of pore size and porosity on mechanical properties and biological response of porous titanium scaffolds. *Mater Sci Eng C* 2017;77:219–28. <https://doi.org/10.1016/j.msec.2017.03.249>.
- [30] Vance A, Bari K, Arjunan A. Investigation of Ti64 sheathed cellular anatomical structure as a tibia implant. *Biomed Phys Eng Express* 2019;5:035008. <https://doi.org/10.1088/2057-1976/ab0bd7>.
- [31] Pattnaik A, Sanket AS, Pradhan S, Sahoo R, Das S, Pany S, Douglas TEL, Dandela R, Liu Q, Rajadas J, Pati S, De Smedt SC, Braeckmans K, Samal SK. Designing of gradient scaffolds and their applications in tissue regeneration. *Biomaterials* 2023;296:122078. <https://doi.org/10.1016/j.biomaterials.2023.122078>.
- [32] Harding A, Pramanik A, Basak AK, Prakash C, Shankar S. Application of additive manufacturing in the biomedical field- a review. *Ann 3D Print Med* 2023;10:100110. <https://doi.org/10.1016/j.stlm.2023.100110>.
- [33] Zhang XY, Fang G, Leeftang S, Zadpoor AA, Zhou J. Topological design, permeability and mechanical behavior of additively manufactured functionally graded porous metallic biomaterials. *Acta Biomater* 2019;84:437–52. <https://doi.org/10.1016/j.actbio.2018.12.013>.
- [34] Hedayati R, Janbaz S, Sadighi M, Mohammadi-Aghdam M, Zadpoor AA. How does tissue regeneration influence the mechanical behavior of additively manufactured porous biomaterials? *J Mech Behav Biomed Mater* 2017;65:831–41. <https://doi.org/10.1016/j.jmbbm.2016.10.003>.
- [35] Bashir S, Fitaihi R, Abdelhakim HE. Advances in formulation and manufacturing strategies for the delivery of therapeutic proteins and peptides in orally disintegrating dosage forms. *Eur J Pharm Sci* 2023;182:106374. <https://doi.org/10.1016/j.ejps.2023.106374>.
- [36] Robinson J, Arjunan A, Baroutaji A, Martí M, Tuñón Molina A, Serrano-Aroca Á, Pollard A. Additive manufacturing of anti-SARS-CoV-2 copper-tungsten-silver alloy. *Rapid Prototyp* 2021. <https://doi.org/10.1108/RPJ-06-2021-0131>. J. ahead-of-p.
- [37] Tony A, Badea I, Yang C, Liu Y, Wells G, Wang K, Yin R, Zhang H, Zhang W. The additive manufacturing approach to polydimethylsiloxane (PDMS) microfluidic devices: review and future directions. *Polymers (Basel)* 2023;15. <https://doi.org/10.3390/polym15081926>.
- [38] Liu Y, Wang W, Zhang LC. Additive manufacturing techniques and their biomedical applications. *Fam Med Commun Heal* 2017;5:286–98. <https://doi.org/10.15212/FMCH.2017.0110>.
- [39] Baroutaji A, Arjunan A, Robinson J, Ramadan M, Abdelkareem MA, Olabi A-G. Metallic Meta-Biomaterial as biomedical implants. In: Olabi A-G, editor. *Encycl. smart mater.* Oxford: Elsevier; 2022. p. 70–80. <https://doi.org/10.1016/B978-0-12-815732-9.00117-0>.
- [40] Benady A, Meyer SJ, Golden E, Dadia S, Katarivas Levy G. Patient-specific Ti-6Al-4V lattice implants for critical-sized load-bearing bone defects reconstruction. *Mater Des* 2023;226:111605. <https://doi.org/10.1016/j.matdes.2023.111605>.
- [41] Mirulla AI, Muccioli GMM, Fratini S, Zaffagnini S, Ingrassia T, Bragonzoni L, Innocenti B. Analysis of different geometrical features to achieve close-to-bone stiffness material properties in medical device: a feasibility numerical study. *Comput Methods Programs Biomed* 2022;221:106875. <https://doi.org/10.1016/j.cmpb.2022.106875>.
- [42] Prada DM, Galvis AF, Miller J, Foster JM, Zavaglia C. Multiscale stiffness characterisation of both healthy and osteoporotic bone tissue using subject-specific data. *J Mech Behav Biomed Mater* 2022;135:105431. <https://doi.org/10.1016/j.jmbbm.2022.105431>.
- [43] Synek A, Ortner L, Pahr DH. Accuracy of osseointegrated screw-bone construct stiffness and peri-implant loading predicted by homogenized FE models relative to micro-FE models. *J Mech Behav Biomed Mater* 2023;140:105740. <https://doi.org/10.1016/j.jmbbm.2023.105740>.
- [44] Meskinfam M. Polymer scaffolds for bone regeneration. *Charact Polym Biomater* 2017;441–75. <https://doi.org/10.1016/B978-0-08-100737-2.00017-0>.
- [45] Alizadeh-Osgouei M, Li Y, Vahid A, Ataee A, Wen C. High strength porous PLA gyroid scaffolds manufactured via fused deposition modeling for tissue-engineering applications. *Smart Mater Med* 2021;2:15–25. <https://doi.org/10.1016/j.smaim.2020.10.003>.
- [46] Shimko DA, Shimko VF, Sander EA, Dickson KF, Nauman EA. Effect of porosity on the fluid flow characteristics and mechanical properties of tantalum scaffolds. *J Biomed Mater Res - Part B Appl Biomater* 2005;73:315–24. <https://doi.org/10.1002/jbm.b.30229>.
- [47] Kumar M, Sharma V. Additive manufacturing techniques for the fabrication of tissue engineering scaffolds: a review. *Rapid Prototyp J* 2021;27:1230–72. <https://doi.org/10.1108/RPJ-01-2021-0011>.
- [48] Vasireddi R, Basu B. Conceptual design of three-dimensional scaffolds of powder-based materials for bone tissue engineering applications. *Rapid Prototyp J* 2015; 21:716–24. <https://doi.org/10.1108/RPJ-12-2013-0123>.
- [49] Kumar M, Mohol SS, Sharma V. A computational approach from design to degradation of additively manufactured scaffold for bone tissue engineering application. *Rapid Prototyp J* 2022;28:1956–67. <https://doi.org/10.1108/RPJ-12-2021-0336>.
- [50] Li J, Xu Z, Wang Q, Hu G, Wang Y. Coupling control of pore size and spatial distribution in bone scaffolds based on a random strategy for additive manufacturing. *Rapid Prototyp J* 2019;25:1030–44. <https://doi.org/10.1108/RPJ-12-2017-0254>.
- [51] Atapour M, Sanaei S, Wei Z, Sheikhleslam M, Henderson JD, Eduok U, Hosein YK, Holdsworth DW, Hedberg YS, Ghorbani HR. In vitro corrosion and biocompatibility behavior of CoCrMo alloy manufactured by laser powder bed fusion parallel and perpendicular to the build direction. *Electrochim Acta* 2023; 445:142059. <https://doi.org/10.1016/j.electacta.2023.142059>.
- [52] Arjunan A, Zahid S, Baroutaji A, Robinson J. 3D printed auxetic nasopharyngeal swabs for COVID-19 sample collection. *J Mech Behav Biomed Mater* 2020: 104175. <https://doi.org/10.1016/j.jmbbm.2020.104175>.
- [53] Cho H, Seo D, Kim D-N. Mechanics of auxetic materials. In: Schmauder S, Chen C-S, Chawla KK, Chawla N, Chen W, Kagawa Y, editors. *Handb. mech. mater.* Singapore: Springer Singapore; 2018. p. 1–25. https://doi.org/10.1007/978-981-10-6855-3_25-1.
- [54] Arjunan A, Baroutaji A, Robinson J, Praveen AS, Pollard A, Wang C. Future directions and requirements for tissue engineering biomaterials. *Ref. Modul. Mater. Sci. Mater. Eng.* Elsevier 2021. <https://doi.org/10.1016/B978-0-12-815732-9.00068-1>.
- [55] Wanniarachchi CT, Arjunan A, Baroutaji A, Singh M. Mechanical performance of additively manufactured cobalt-chromium-molybdenum auxetic meta-biomaterial bone scaffolds. *J Mech Behav Biomed Mater* 2022;134:105409. <https://doi.org/10.1016/j.jmbbm.2022.105409>.
- [56] Gibson LJ, Ashby MF. *Cellular solids: structure and properties*. 2nd ed. Cambridge University Press; 1997.
- [57] Lee J, Yoo JJ, Atala A, Lee SJ. The effect of controlled release of PDGF-BB from heparin-conjugated electrospun PCL/gelatin scaffolds on cellular bioactivity and infiltration. *Biomaterials* 2012;33:6709–20. <https://doi.org/10.1016/j.biomaterials.2012.06.017>.
- [58] Kolken HMA, Lietaert K, van der Sloten T, Pouran B, Meynen A, Van Loock G, Weinans H, Schemys L, Zadpoor AA. Mechanical performance of auxetic meta-biomaterials. *J Mech Behav Biomed Mater* 2020;104. <https://doi.org/10.1016/j.jmbbm.2020.103658>.
- [59] Kolken HMA, Janbaz S, Leeftang SMA, Lietaert K, Weinans HH, Zadpoor AA. Rationally designed meta-implants: a combination of auxetic and conventional meta-biomaterials. *Mater Horizons* 2018;5:28–35. <https://doi.org/10.1039/C7MH00699C>.
- [60] Schemitsch EH. Size matters: defining critical in bone defect size! *J Orthop Trauma* 2017;31:S20–2. <https://doi.org/10.1097/BOT.0000000000000978>.
- [61] Utomo DN, Hernugrahanto KD, Edward M, Widhiyanto L, Mahyudin F. Combination of bone marrow aspirate, cancellous bone allograft, and platelet-rich plasma as an alternative solution to critical-sized Diaphyseal bone defect: a case series. *Int J Surg Case Rep* 2019;58:178–85. <https://doi.org/10.1016/j.ijscr.2019.04.028>.
- [62] Christou C, Oliver RA, Pelletier MH, Walsh WR. Ovine model for critical-size tibial segmental defects. *Comp Med* 2014;64:377–85. <https://www.ncbi.nlm.nih.gov/pubmed/25402178>.
- [63] Nikkhah H, Baroutaji A, Olabi AG. Crashworthiness design and optimisation of windowed tubes under axial impact loading. *Thin-Walled Struct* 2019;142: 132–48. <https://doi.org/10.1016/j.tws.2019.04.052>.
- [64] Lenth RV. Response-surface methods in R, using RSM. *J Stat Softw* 2009;32:1–17. <https://doi.org/10.18637/jss.v032.i07>.
- [65] Lorza RL, Calvo MAM, Labari CB, Fuente PJR. Using the multi-response method with desirability functions to optimize the Zinc electroplating of steel screws. *Metals (Basel)* 2018;8:1–20. <https://doi.org/10.3390/met8090711>.
- [66] Arjunan A, Demetriou M, Baroutaji A, Wang C. Mechanical performance of highly permeable laser melted Ti6Al4V bone scaffolds. *J Mech Behav Biomed Mater* 2020;102:103517. <https://doi.org/10.1016/j.jmbbm.2019.103517>.
- [67] INTERNATIONAL STANDARD verification of static uniaxial testing — Calibration and verification of the, 2018 (2018).
- [68] Bari K, Arjunan A. Extra low interstitial titanium based fully porous morphological bone scaffolds manufactured using selective laser melting. *J Mech Behav Biomed Mater* 2019;95:1–12. <https://doi.org/10.1016/j.jmbbm.2019.03.025>.
- [69] Ahmed A, Majeed A, Atta Z, Guozhu G. Dimensional quality and distortion analysis of thin-walled alloy parts of AlSi10Mg manufactured by selective laser melting. *J Manuf Mater Process* 2019;3:51. <https://doi.org/10.3390/jmmp3020051>.
- [70] Zadpoor AAAA. *Mechanics of additively manufactured biomaterials*. Elsevier Ltd; 2017. <https://doi.org/10.1016/j.jmbbm.2017.03.018>.
- [71] Tan JH, Wong WLE, Dalgarno KW. An overview of powder granulometry on feedstock and part performance in the selective laser melting process. *Addit Manuf* 2017;18:228–55. <https://doi.org/10.1016/j.addma.2017.10.011>.
- [72] Weißmann V, Drescher P, Bader R, Seitz H, Hansmann H, Laufer N. Comparison of single Ti 6 Al 4 V struts made using selective laser melting and electron beam melting subject to part orientation. *Metals (Basel)* 2017. <https://doi.org/10.3390/met7030091>.
- [73] Sing SL, Yeong WY, Wiria FE, Tay BY. Characterization of titanium lattice structures fabricated by selective laser melting using an adapted compressive test method. *Exp Mech* 2016;56:735–48. <https://doi.org/10.1007/s11340-015-0117-y>.
- [74] De Wild M, Schumacher R, Mayer K, Schkommodau E, Thoma D, Bredell M, Kruse Gujer A, Grätz KWKW, Weber FEFE. Bone regeneration by the osteoconductivity of porous titanium implants manufactured by selective laser melting: a histological and micro computed tomography study in the rabbit. *Tissue Eng - Part A*. 2013;19:2645–54. <https://doi.org/10.1089/ten.tea.2012.0753>.
- [75] Liu F, Mao Z, Zhang P, Zhang DZ, Jiang J, Ma Z. Functionally graded porous scaffolds in multiple patterns: new design method, physical and mechanical

- properties. *Mater Des* 2018;160:849–60. <https://doi.org/10.1016/j.matdes.2018.09.053>.
- [76] Speirs M, Van Hooreweder B, Van Humbeeck J, Kruth J-PP. Fatigue behaviour of NiTi shape memory alloy scaffolds produced by SLM, a unit cell design comparison. *J Mech Behav Biomed Mater* 2017;70:53–9. <https://doi.org/10.1016/j.jmbbm.2017.01.016>.
- [77] Wang L, Kang J, Sun C, Li D, Cao Y, Jin Z. Mapping porous microstructures to yield desired mechanical properties for application in 3D printed bone scaffolds and orthopaedic implants. *Mater Des* 2017;133:62–8. <https://doi.org/10.1016/j.matdes.2017.07.021>.
- [78] Taniguchi N, Fujibayashi S, Takemoto M, Sasaki K, Otsuki B, Nakamura T, Matsushita T, Kokubo T, Matsuda S. Effect of pore size on bone ingrowth into porous titanium implants fabricated by additive manufacturing: an in vivo experiment. *Mater Sci Eng C*. 2016;59:690–701. <https://doi.org/10.1016/j.msec.2015.10.069>.
- [79] Wahid Z, Ariffin MKAM, Baharudin BHTT, Ismail MIS, Mustapha F. Abaqus simulation of different critical porosities cubical scaffold model. *IOP Conf Ser Mater Sci Eng* 2019;530:012018. <https://doi.org/10.1088/1757-899X/530/1/012018>.
- [80] Salimon A, Bréchet Y, Ashby MF, Greer AL. Potential applications for steel and titanium metal foams. *J Mater Sci* 2005;40:5793–9. <https://doi.org/10.1007/s10853-005-4993-x>.
- [81] Favre J, Lohmuller P, Piotrowski B, Kenzari S, Laheurte P, Meraghni F. A continuous crystallographic approach to generate cubic lattices and its effect on relative stiffness of architected materials. *Addit Manuf* 2018;21:359–68. <https://doi.org/10.1016/j.addma.2018.02.020>.
- [82] Bobbio LD, Qin S, Dunbar A, Michaleris P, Beese AM. Characterization of the strength of support structures used in powder bed fusion additive manufacturing of Ti-6Al-4V. *Addit Manuf* 2017;14:60–8. <https://doi.org/10.1016/j.ADDMA.2017.01.002>.
- [83] Savio G, Rosso S, Curtarello A, Meneghello R, Concheri G. Implications of modeling approaches on the fatigue behavior of cellular solids. *Addit Manuf* 2019;25:50–8. <https://doi.org/10.1016/j.addma.2018.10.047>.
- [84] Stuhle L, Wold S. Analysis of variance (ANOVA). *Chemom Intell Lab Syst* 1989;6: 259–72. [https://doi.org/10.1016/0169-7439\(89\)80095-4](https://doi.org/10.1016/0169-7439(89)80095-4).
- [85] G.S.B.T.-S.T. for Molugaram K, Rao GS. Chapter 11 - ANOVA (Analysis of Variance). In: Molugaram K, Rao TE, editors. Butterworth-Heinemann; 2017. p. 451–62. <https://doi.org/10.1016/B978-0-12-811555-8.00011-8>.
- [86] Rossi F, Mirtchev V. Chapter 4 - analysis of variance (ANOVA). In: Rossi F, Mirtchev V, editors. *Stat. food sci.* San Diego: Academic Press; 2016. p. 19–29. <https://doi.org/10.1016/B978-0-12-417179-4.00004-4>.
- [87] Arjunan A, Singh M, Baroutaji A, Wang C. Additively manufactured AlSi10Mg inherently stable thin and thick-walled lattice with negative Poisson's ratio. *Compos Struct* 2020;247:112469. <https://doi.org/10.1016/j.compstruct.2020.112469>.
- [88] Wang Z, Han L, Zhou Y, Cai J, Sun S, Ma J, Wang W, Li X, Ma L. The combination of a 3D-Printed porous Ti-6Al-4V alloy scaffold and stem cell sheet technology for the construction of biomimetic engineered bone at an ectopic site. *Mater Today Bio* 2022;16:100433. <https://doi.org/10.1016/j.mtbio.2022.100433>.
- [89] Mohandesnezhad S, Monfared MH, Samani S, Farzin A, Poursamar SA, Ai J, Ebrahimi-barough S, Azami M. 3D-printed bioactive Chitosan/Alginate /Hardystonite scaffold for bone tissue engineering: synthesis and characterization. *J Non Cryst Solids* 2023;609:122261. <https://doi.org/10.1016/j.jnoncrystol.2023.122261>.
- [90] Dai K, Yang Z, Ding L, Yang Z, Hang F, Cao X, Chen D, Zhao F, Chen X. 3D-printed strontium-doped BG-CaSiO₃-HA composite scaffolds promote critical bone defect repair by improving mechanical strength and increasing osteogenic activity. *Ceram Int* 2023. <https://doi.org/10.1016/j.ceramint.2023.03.095>.
- [91] Foroughi AH, Valeri C, Jiang D, Ning F, Razavi M, Razavi MJ. Understanding compressive viscoelastic properties of additively manufactured PLA for bone-mimetic scaffold design. *Med Eng Phys* 2023;103972. <https://doi.org/10.1016/j.medengphy.2023.103972>.
- [92] Fan J, Zhang L, Wei S, Zhang Z, Choi S-K, Song B, Shi Y. A review of additive manufacturing of metamaterials and developing trends. *Mater Today*. 2021;50: 303–28. <https://doi.org/10.1016/j.mattod.2021.04.019>.
- [93] Hu LL, Zhou MZ, Deng H. Dynamic indentation of auxetic and non-auxetic honeycombs under large deformation. *Compos Struct* 2019;207:323–30. <https://doi.org/10.1016/J.COMPSTRUCT.2018.09.066>.
- [94] Ju J, Summers JD. Compliant hexagonal periodic lattice structures having both high shear strength and high shear strain. *Mater Des* 2011;32:512–24. <https://doi.org/10.1016/j.matdes.2010.08.029>.
- [95] Xiang J, Du J. Energy absorption characteristics of bio-inspired honeycomb structure under axial impact loading. *Mater Sci Eng A* 2017;696:283–9. <https://doi.org/10.1016/j.msea.2017.04.044>.
- [96] Gunantara N. A review of multi-objective optimization: methods and its applications. *Cogent Eng* 2018;5:1–16. <https://doi.org/10.1080/23311916.2018.1502242>.
- [97] P. Cortez, Multi-objective optimization, (2014) 99–117. [10.1007/978-3-319-08263-9_6](https://doi.org/10.1007/978-3-319-08263-9_6).
- [98] A. Ning, J.R.R.A. Martins, *Engineering design optimization*, 2020.
- [99] Javadi AA, Faramarzi A, Farmani R. Design and optimization of microstructure of auxetic materials. *Eng Comput* 2012;29:260–76. <https://doi.org/10.1108/02644401211212398>.
- [100] Cao L, Dolovich AT, Schwab AL, Herder JL, Zhang W(Chris). Toward a unified design approach for both compliant mechanisms and rigid-body mechanisms: module optimization. *J Mech Des* 2015;137:122301. <https://doi.org/10.1115/1.4031294>.